

Research Article

Open Access



Smart wearable photonic array biosensor for human sweat analysis

Saddam Hussain, Qasem Ramadan, Mohammed Zourob*

Department of Chemistry, College of Science, Alfaisal University, Riyadh, Al-Maather 11533, Saudi Arabia.

*Correspondence to: Prof. Mohammed Zourob, Department of Chemistry, College of Science, Alfaisal University, Al Zahrawi Street, Riyadh, Al-Maather 11533, Saudi Arabia. E-mail: mzourob@alfaisal.edu

How to cite this article: Hussain, S.; Ramadan, Q.; Zourob, M. Smart wearable photonic array biosensor for human sweat analysis. *Soft Sci.* 2025, 5, 21. <https://dx.doi.org/10.20517/ss.2025.02>

Received: 11 Jan 2025 **First Decision:** 6 Feb 2025 **Revised:** 11 Feb 2025 **Accepted:** 27 Feb 2025 **Published:** 27 Apr 2025

Academic Editors: Carlo Massaroni, Roozbeh Ghaffari, Nae-Eung Lee **Copy Editor:** Pei-Yun Wang **Production Editor:** Pei-Yun Wang

Abstract

Cholesteric liquid crystal networks (CLCNs) intertwined with interpenetrating polymer network (IPN) hydrogels have emerged as a promising platform for the development of optical photonic sensors. However, the integration of a multiplex biosensor within a flexible substrate for real-time human sweat analysis remains a significant challenge. Herein, we present a novel flexible CLCN-IPN-based sensor array, embedded within a soft wearable microfluidic patch, designed for the continuous monitoring of human sweat. This innovative biosensor allows optical detection of glucose, urea, and lactate with impressive limits of detection: 0.31 mM for glucose, 0.273 mM for urea, and 3.11 mM for lactate. The wearable array biosensor enables real-time analysis of sweat, offering results that can be interpreted with the naked eye, eliminating the need for complex instruments. This approach to epidermal health monitoring has the potential to inspire new advancements in wearable sensor devices, contributing to the future of smart healthcare applications.

Keywords: Smart photonic structures, soft wearable patch, optical sweat monitoring, non-invasive diagnostics, multiplex biosensing platform

INTRODUCTION

Sweat has been recognized as a health indicator since ancient times, with early physicians observing changes in sweat odor, color, and quantity during illness and physical exertion^[1,2]. For example, Hippocrates, the



© The Author(s) 2025. **Open Access** This article is licensed under a Creative Commons Attribution 4.0 International License (<https://creativecommons.org/licenses/by/4.0/>), which permits unrestricted use, sharing, adaptation, distribution and reproduction in any medium or format, for any purpose, even commercially, as long as you give appropriate credit to the original author(s) and the source, provide a link to the Creative Commons license, and indicate if changes were made.



ancient Greek physician, linked sweat to fever and other health conditions^[3]. However, systematic analysis did not begin until the 19th century, when researchers linked basic sweat components such as salt (sodium chloride) to functions such as temperature regulation^[4-6]. The early 20th century marked significant progress in sweat analysis, focusing on electrolyte content such as sodium and potassium, which improved the understanding of conditions such as dehydration and heat-related illnesses. In the 1950s, sweat analysis took a major step forward with the introduction of the sweat chloride test for diagnosing cystic fibrosis (CF)^[7,8], as researchers discovered abnormally high chloride levels in sweat from CF patients. This test remains a standard diagnostic tool^[9,10]. The late 20th century saw significant technological advancements, including the development of gas chromatography, mass spectrometry, and ion-selective electrodes, enabling detailed analysis of sweat for a broader range of substances, such as metabolites, hormones, and drugs^[11-16]. The 1980s and 1990s introduced sweat patches for monitoring substance use, offering a new approach to drug testing^[17-19]. In the 21st century, the field expanded with wearable sweat sensors incorporating electronics and optical materials to continuously track biomarkers such as glucose, lactate, and electrolytes in real time^[13,19-22]. These innovations have made sweat analysis a promising non-invasive alternative for monitoring health, fitness, and chronic diseases, as modern devices can detect multiple analytes simultaneously, providing valuable insights for diagnostics and personalized medicine.

Wearable biosensors have emerged as promising tools for non-invasive monitoring of physiological parameters, with sweat analysis being particularly advantageous due to its ease of collection and wealth of biological information^[23]. Traditional sweat sensors, including electrochemical^[24,25], and colorimetric paper-based systems, have shown potential but face significant limitations related to sensitivity, selectivity, and mechanical robustness. Electrochemical sensors, while highly sensitive, often suffer from interference due to the complex composition of sweat, requiring frequent recalibration, which reduces their long-term reliability. Additionally, these sensors often incorporate rigid conductive wires and require an external power supply, complicating the design and assembly, and making them susceptible to mechanical failure due to the natural stretching of human skin^[24,26-28]. Colorimetric paper-based sensors rely on changes in color intensity rather than a full wavelength shift, making the results difficult to interpret with the naked eye^[27]. Textile-based colorimetric sensors have also been developed for lactate sensing in sweat, but the intensity-based color change requires sophisticated instrumentation to correlate accurately with lactate concentrations^[29]. Fluorescent dye-based sweat sensors face additional challenges, such as low efficiency, cross-contamination of sweat, and irreversible color changes, limiting their practicality^[30,31]. Recent advancements in microfluidic technology have significantly improved sweat sensor performance by overcoming these limitations^[32-34]. Microfluidic devices address issues such as inefficient fluid collection, cross-contamination, and irreversible detection signals seen in traditional sensors^[35,36]. Conventional methods, often reliant on absorbent materials such as paper or textiles, are prone to mixing old and new sweat samples, which hinders accurate measurements^[37,38]. Additionally, backflow and contamination of chemical reagents compromise sensor reliability. However, by incorporating super-wettable materials and surface modifications, microfluidic systems can channel sweat more efficiently^[39]. Moreover, microfluidic devices enable real-time monitoring of sweat loss and chemical concentrations by utilizing the natural secretion pressure from sweat glands and the capillary forces within microchannels. This enhances fluid collection efficiency while minimizing evaporation and contamination. These innovations not only allow for dynamic feedback and intermittent analysis but also provide a level of control and reliability that traditional sensors lack. As a result, microfluidic sweat sensors have emerged as powerful tools for continuous health monitoring and real-time physiological assessments.

Cholesteric liquid crystal network (CLCN) is a class of one-dimensional photonic materials that reflect only circularly polarized (CP) light based on the handedness of their helical structure^[40]. This unique property is

due to the photonic bandgap (λ_{PBG}) exhibited by CLCNs, which can be shifted to different wavelengths in response to external stimuli such as pH^[41,42], temperature^[43], mechanical stress^[44], or organic solvents^[45]. To enhance the hydrophilicity and responsiveness of CLCNs in aqueous environments, researchers have developed interpenetrating polymer networks (IPNs) integrated with CLCNs, making them ideal for biosensing applications^[46]. Several CLCN-IPN films have been fabricated on glass substrates for the analysis of human body fluids^[47-50]. The IPN typically consists of a weak polyelectrolyte hydrogel, which can undergo volumetric changes when exposed to external stimuli. These changes in volume directly alter the helical pitch of the CLCN, resulting in a visible color shift. Specifically, an increase in volume induces a red shift, while a decrease (or shrinkage) causes a blue shift. Unlike traditional dye-based sensors that rely on chemical colors which can degrade over time, CLCN-IPNs provide stable photonic colors that do not fade^[51]. Their solid structure and durability allow them to remain functional across a wide range of temperatures, making them long-lasting and reliable for various biosensing applications.

Despite significant progress in wearable photonic biosensors, many existing technologies still face challenges in terms of usability, real-time monitoring, and integration into practical applications. In response to these limitations, we have developed a novel optical photonic sensor based on a CLCN-IPN system, seamlessly integrated into a soft wearable microfluidic device. Unlike conventional colorimetric sweat sensors that rely on intensity-based dye changes, our system utilizes structural photonic color shifts that provide stable, real-time detection without requiring an external power source or electronic components. A key innovation of our device lies in its enzyme-functionalized CLCN-IPN hydrogel network, which ensures high selectivity, mechanical flexibility, and durability for prolonged wear. The microfluidic polydimethylsiloxane (PDMS) patch is carefully designed to enable efficient sweat collection, controlled fluid flow, and reduced contamination risk, ensuring accurate and interference-free biomarker detection. Furthermore, the dynamic λ_{PBG} shifts in response to biomarker concentration changes allow for intuitive, naked-eye detection, eliminating the need for sophisticated optical instrumentation. By combining optical photonic sensing with microfluidic engineering, our platform bridges the gap between laboratory-based detection methods and practical, on-body health monitoring, offering a scalable, user-friendly, and cost-effective solution for real-time sweat analysis. This advancement represents a significant step forward in wearable biosensing, providing a battery-free, power-independent, and non-invasive diagnostic tool for monitoring glucose, lactate, and urea in human sweat.

EXPERIMENTAL

Materials

Materials 1,4-Bis-[4-(6-acryloyloxyhexyloxy)benzoyloxy]-2-methylbenzene (RM82), 4-Methoxyphenyl 4-((6-(acryloyloxy)hexyl)oxy)benzoate (RM105), (3R,3aS,6aS)-hexahydrofuro[3,2-b]furan-3,6-diyl bis(4-(4-((4-(acryloyloxy)butoxy)carbonyloxy)benzoyloxy)benzoate) (DK756), and 4-Cyano-4'-pentylbiphenyl (5CB) were sourced from Daken Chemical Limited, China. Trichloro(1H,1H,2H,2H-perfluorooctyl)silane (PFOTS), 3-(trimethoxysilyl)propyl methacrylate (TMSPMA), acrylic acid (AA), 2-(dimethylamino)ethyl methacrylate (DMAEMA), tri(propylene glycol) diacrylate (TPGDA), phenylbis(2,4,6-trimethylbenzoyl)phosphine oxide (PI), N-(3-dimethylaminopropyl)-N'-ethylcarbodiimide hydrochloride (EDC), N-hydroxysuccinimide (NHS), magnesium chloride (MgCl_2), acetone, and ethanol were procured from Sigma Aldrich (USA). Urea, urease, sodium L-lactate, lactate oxidase (LOx), glucose, and glucose oxidase were also obtained from Sigma Aldrich. Calcium chloride dihydrate ($\text{CaCl}_2 \cdot 2\text{H}_2\text{O}$) and sodium chloride (NaCl) were received from Merck, USA. Potassium chloride (KCl) was obtained from PanReac, Spain. All chemicals were used as received without further purification unless otherwise noted. Glass slides (Euruslide, United Kingdom) were pre-cleaned with water and ethanol before use. Milli-Q water was employed for all reagent preparations.

Preparation of wearable photonic array biosensor films

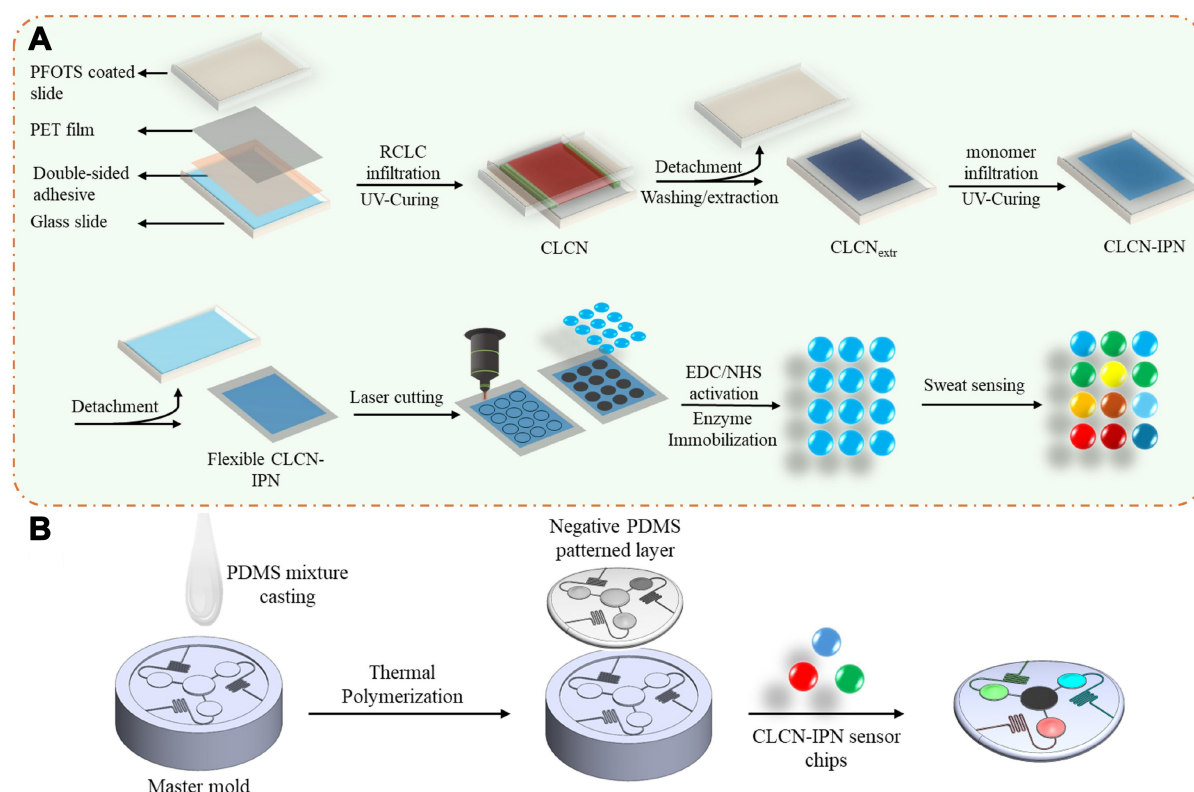
Scheme 1A illustrates the sequential fabrication of circular CLCN-IPN biosensor films. First, microscopic glass slides were cut into 4 cm pieces, cleaned with water and ethanol, and dried using an air blower. Clean polyethylene terephthalate (PET) films were adhered to the glass slides using double-sided tape. The PET films were then washed with water and ethanol, followed by drying with an air blower, and referred to as the “bottom glass slide”. Both the bottom and top glass slides underwent surface functionalization. They were treated in an oxygen plasma cleaner (PC-002-CE, USA) connected to a vacuum pump (MM71A4, Valtoro Motori, Italy) for 15 min. After oxygen plasma treatment, the top glass slide was functionalized with a PFOTS mixture by placing it in a sealed petri dish containing FPOTS mixture and heating at 70 °C for 5 h. Meanwhile, the bottom glass slide was coated with a TMSPMA mixture using a spin coater (Laurell Tech Corporation, USA) at 2,000 rpm for 1 min, followed by baking at 65 °C for 5 h. Both slides were then assembled using a 20 µm thick plastic spacer, creating a 20 µm gap between them. This gap was filled with the reactive cholesteric liquid crystal (CLC) mixture (composition provided in **Supplementary Table 1** of the supporting information) via capillary forces. Once infiltration was complete, the assembly was exposed to ultraviolet (UV) photopolymerization for 20 min using a UV lamp (DR-301C, China). After polymerization, the top glass slide was removed, leaving the CLCN film fixed to the bottom glass slide. The CLCN film was thoroughly washed with acetone to remove any nonreactive 5CB. Next, a hydrogel monomer mixture (composition provided in the supporting information in **Supplementary Table 2**) was applied to the surface of the CLCN film and allowed to infiltrate for 30 min. The film was then exposed to UV curing for 30 min to establish a stable IPN. The glass slide and double-sided tape were removed from the flexible CLCN-IPN film, which remained adhered to the PET substrate. The flexible film was cut into 5 mm diameter circular shapes using a laser cutter (Beambox, Flux, Taipei, Taiwan) and the Beam Studio software. To immobilize enzymes on the CLCN-IPN circular films, the films were treated with an EDC/NHS mixture [1 M EDC-HCl and 2 M NHS mixed at a 1:1 (v/v) ratio] in a glass vial for 2 h. After activation, the films were wiped with tissue paper and proceeded for enzyme immobilization. The concentrations and types of enzymes used are detailed in the corresponding sections. After enzyme immobilization, the circular CLCN-IPN films were washed with deionized (DI) water and prepared for sensing applications. The color shift in the CLCN-IPN biosensor films corresponds to the concentration of the target analyte. **Scheme 1B** describes the preparation of the soft wearable device. A mold was initially created using a SIGA MAX UV 3D printer (NSW, Australia). The PDMS precursor was prepared by mixing Sylgard 184 silicone elastomer base and curing agent at a 9:1 (w/w) ratio. The PDMS precursor was then poured into the resin mold, covered with a polymethylmethacrylate (PMMA) hard sheet, and baked at 60 °C for 24 h. Once cured, a uniform patterned PDMS layer with clear microchannels was peeled off from the mold. The circular CLCN-IPN biosensor films were then placed into the reservoirs of the patterned PDMS layer (details provided in Section “Urea detection by circular photonic CLCN-IPN biosensor film”). The fabricated wearable photonic array biosensor was stored at -8 °C in a refrigerator.

Preparation of artificial sweat

Artificial sweat was prepared based on a previously reported method. The components included sodium lactate (20 mM), D-glucose (0.5 mM), sodium chloride (80 mM), potassium chloride (9 mM), calcium chloride (1 mM), urea (21 mM), iron (II) chloride (0.01 mM), and magnesium chloride hexahydrate (0.3 mM), all dissolved in a buffer solution at pH 6. Varying concentrations of glucose, urea, or lactate were achieved by adjusting the corresponding component while maintaining the concentrations of the other ingredients constant.

Off-body and on-body sweat analysis

For off-body sweat analysis, a syringe pump (WPI, 230, Germany) was used. A round PDMS layer with a diameter of 35 mm was fabricated, and a hole was punched in its center to connect it to the syringe pump



Scheme 1. (A) Sequential fabrication of CLCN-IPN biosensor films; (B) Preparation of the patterned layer for the wearable patch using molding technology. CLCN: Cholesteric liquid crystal network; IPN: interpenetrating polymer network.

via a Tygon tube. The wearable biosensor chip was secured to the PDMS layer using medical-grade double-sided tape, aligning the sweat collection chamber of the biosensor with the puncture hole as shown in [Supplementary Movie 1](#). Artificial sweat was injected into the sweat collection chamber at a controlled flow rate. For on-body sweat analysis, the wearable biosensor chip was attached to the arm of a healthy 28-year-old female volunteer using medical-grade adhesive. After 30 min of exercise, the biosensor chip filled with sweat. The photographs were taken 2 h later, and UV-Visible (Vis) spectra were recorded.

Measurements and characterizations

UV-Vis absorbance measurements were performed using a spectrofluorometer (FS5, EHS4 7DQ, Livingston, UK) over the wavelength range of 300–900 nm. A custom-built glass chamber was employed, which was constructed by sandwiching two glass slides with a double-sided adhesive tape, creating a 2 mm gap between them. The CLCN-IPN chip was placed inside the chamber, which was then filled with DI water, and the chamber was aligned perpendicular to the spectrofluorometer beam. To capture polarized UV-Vis spectra, right-hand (RHCP) and left-hand CP (LHCP) glass filters were inserted in the light path. The same setup was used for imaging under CP light. A smartphone camera (Galaxy A73, Samsung, South Korea) was used to capture images. The limit of detection (LOD) was determined using $\text{LOD} = 3.3 \times (\text{standard deviation of triplicate blank measurements}) / (\text{slope of the calibration curve})$. This approach ensures that the LOD reflects the lowest concentration of the analyte that can be reliably distinguished from the background noise, considering the variability in the blank measurements. Furthermore, the cross-sectional surface of the photonic layer structure of the CLCN film was analyzed using scanning electron microscopy (SEM) with a field emission microscope (JSMIT500HR, TouchScope, JEOL, Pleasanton, CA, USA). Prior to imaging, a 4 nm platinum coating was applied to the sample to improve image resolution.

and enhance surface clarity during SEM observation.

RESULTS AND DISCUSSION

Preparation of circular photonic CLCN-IPN biosensor film

The CLCN-IPN biosensor film was fabricated on a flexible PET substrate. The functionalized PET film contains reactive groups that form covalent bonds with the reactive CLC mixture. The fabricated CLCN-IPN biosensor film was characterized by using photographic images and UV-Vis spectroscopy. [Supplementary Figure 1A](#) shows the photographic images of the CLCN film under unpolarized, LHCP, and RHCP light. The film appears colored under unpolarized and RHCP light, while no color is visible under LHCP light, indicating the successful development of a right-handed (RH) helical structure in the CLCN. After the extraction of nonreactive 5CB, a blue shift in the film's color was observed, while the RH helical arrangement remained intact. [Supplementary Figure 1B and C](#) shows the corresponding UV-Vis spectra under the respective polarizers, where the photonic band gap (λ_{PBG}) disappears in the spectra recorded under the LHCP light beam. [Supplementary Figure 1D](#) illustrates the λ_{PBG} values for CLCN, CLCN_{extr}, and CLCN-IPN films. The initial λ_{PBG} of the CLCN at 585 nm shifted to 415 nm for CLCN_{extr} and increased to 445 nm for CLCN-IPN. The blue shift in CLCN_{extr} confirms the removal of 5CB, which reduced the helical pitch and resulted in the blue shift. The subsequent red shift after IPN development demonstrates the successful formation of the IPN within the CLCN-IPN film. Furthermore, we evaluated the flexibility of the CLCN-IPN film. [Supplementary Figure 2](#) demonstrates the film's ability to undergo bending, rolling, and squeezing, followed by its restoration to its original shape. These results confirm that the CLCN-IPN film possesses sufficient flexibility to conform to the contours of human skin, making it ideal for wearable applications. Additionally, the film's resilience ensures that it can withstand regular human movements, such as arm motions, without experiencing damage or loss of functionality. The CLCN-IPN film prepared on the PET substrate was laser-cut into circular shapes with a 5 mm diameter. [Supplementary Figure 3](#) presents photographic images of the circular CLCN-IPN films, cut from the original parent film. [Supplementary Movie 2](#) demonstrates the live cutting process using the laser cutting machine.

Furthermore, the developed photonic structure was analyzed using SEM to confirm the formation of a well-aligned one-dimensional photonic structure. As shown in [Supplementary Figure 4](#), the SEM image of the cross-sectional surface of the CLCN_{extr} film reveals its distinct layered architecture. The pitch, defined as the distance between two corresponding layers, was measured at ten different locations across the sample. The calculated average pitch was 258 nm. This value closely corresponds to the λ_{PBG} observed in the UV-Vis spectrum of the CLCN_{extr} film. The consistency between the pitch measurement and the λ_{PBG} indicates a well-ordered photonic structure, further confirming the precise development and alignment of the CLCN_{extr} layers. These findings validate the successful fabrication of a highly organized CLCN photonic structure.

Urea detection by circular photonic CLCN-IPN biosensor film

The CLCN-IPN biosensor film for urea detection was fabricated using a 4% RHCLC and AA mixture. Urease, an enzyme that catalyzes the hydrolysis of urea into carbon dioxide (CO₂) and ammonium hydroxide (NH₄OH), plays a crucial role in the sensing mechanism. As NH₄OH is produced, the pH of the local environment increases, causing a disruption in the hydrogen bonding between the carboxylic acid groups in the IPN-poly (acrylic acid) (PAA). This leads to an increase in the ionization of carboxylic groups, which makes the network more hydrophilic and results in swelling due to the influx of water molecules. The expansion of the IPN-PAA increases its volume, which directly influences the helical pitch of the CLC, causing a red shift in the λ_{PBG} , as depicted in [Figure 1A](#). To optimize the amount of immobilized urease for maximum sensitivity, circular CLCN-IPN films were first activated with EDC/NHS chemistry, which facilitates the formation of covalent bonds between urease and the carboxyl groups on the surface of the film. Urease was immobilized at different concentrations (C_{urease}) by applying a 10 μL aqueous solution of

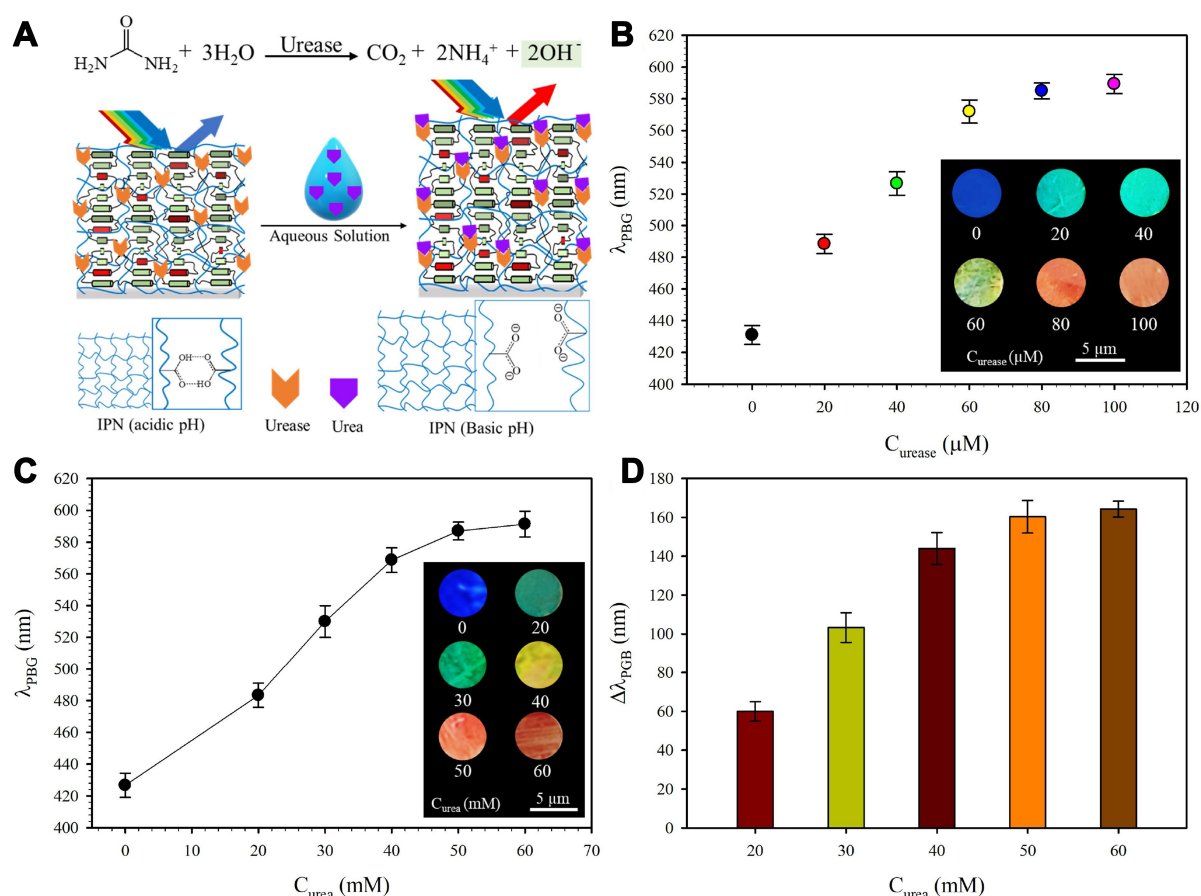


Figure 1. (A) Mechanism of urea sensing using the CLCN-IPN_{urease} film; (B) λ_{PBG} values plotted against different concentrations of urease (C_{urease}); insets show real photographs of CLCN-IPN_{urease} circular films, with numbers indicating the urease concentration in μM ; (C) Redshift of λ_{PBG} values as C_{urea} increases; insets display photographs of CLCN-IPN_{urease} films tested with corresponding urea concentrations; (D) Bar graph illustrating $\Delta\lambda_{\text{PBG}}$ as a function of C_{urea} . Error bars in (B-D) represent the standard deviation from triplicate experiments. CLCN: Cholesteric liquid crystal network; IPN: interpenetrating polymer network.

varying concentrations onto the activated surface. After a 2-hour incubation, the films were thoroughly washed with DI water. Figure 1B shows the λ_{PBG} shift from 435 to 587 nm with increasing C_{urease} concentrations, indicating a direct relationship between urease loading and the optical response of the film. Our goal was to enable the sensor to cover the full visible spectrum, ranging from blue to red. The inset photographs clearly show a progression of color shifts from blue to green, yellow, and orange-red. The sensing capability of the films was tested using a 50 mM urea solution. Supplementary Figure 5A presents the UV-Vis spectra of CLCN-IPN films immobilized with different concentrations of urease (CLCN-IPN_{urease}), revealing a consistent red shift up to a C_{urease} concentration of 80 μM . Supplementary Figure 5B displays the corresponding change in λ_{PBG} ($\Delta\lambda_{\text{PBG}}$), showing a linear increase until it reaches a maximum shift of 157 nm at a C_{urease} concentration of 80 μM , after which the response plateaus, indicating equilibrium. This data confirms that 80 μM is the optimal concentration of urease, providing a robust and responsive sensing platform.

The response of the CLCN-IPN_{urease} film was evaluated by exposing it to different concentrations of urea (C_{urea}) in aqueous solutions. Figure 1C presents photographs and the corresponding λ_{PBG} values for the CLCN-IPN_{urease} film, measured 2 h after the addition of 10 μL of C_{urea} solutions. The results show a linear

increase in λ_{PBG} values as the urea concentration rises, with the shift plateauing when the C_{urea} reaches 50 mM. This linear trend highlights the sensor's sensitivity to urea concentration changes, providing a reliable optical response. **Figure 1D** shows the $\Delta\lambda_{\text{PBG}}$, with a maximum shift of 154 nm recorded, demonstrating the significant modulation in photonic properties due to the swelling of the IPN upon urea hydrolysis. Importantly, the typical concentration of urea in human sweat is approximately 22 mM for a healthy individual^[52]. At this physiological concentration, the sensor maintains a green color, indicating normal urea levels. However, as the concentration increases beyond normal physiological ranges, the sensor exhibits a distinct color shift from green to yellow, and ultimately to red, signaling elevated urea levels. This colorimetric change provides a straightforward visual cue for real-time urea monitoring. **Supplementary Figure 5C** presents the UV-Vis spectra corresponding to the color shifts, further confirming the λ_{PBG} shifts across different urea concentrations. The LOD for the CLCN-IPN_{urease} film was calculated to be 0.273 mM, with a linear range 0.7–50 mM, as derived from the data in **Supplementary Figure 5D**. The linear standard curve in **Supplementary Figure 5D** was used to quantify the urea concentrations, demonstrating the sensor's high sensitivity and applicability for detecting even small variations in urea levels. The high sensitivity, combined with the wide detection range, makes this biosensor a promising candidate for wearable applications in health monitoring, particularly for tracking urea levels in sweat as an indicator of hydration status or kidney function.

Lactate sensing by circular photonic CLCN-IPN biosensor film

The circular photonic CLCN-IPN biosensor film was fabricated using a 4% reactive CLC mixture, with the IPN constructed from AA-co-DMAEMA. The IPN structure was specifically designed to facilitate dual functionality: 20% of the AA units were utilized for the covalent immobilization of LOx enzymes, while the remaining DMAEMA units were responsible for inducing a volumetric response to changes in pH. LOx catalyzes the oxidation of L-lactate to pyruvate, a reaction that decreases the local pH. This is due to the pKa values of lactate (3.86) and pyruvate (2.49), meaning the oxidation reaction produces a more acidic environment, as illustrated in **Figure 2A**. For this reason, poly-DMAEMA was chosen as the hydrogel matrix, as it is responsive to acidic pH, undergoing swelling and increasing in volume under such conditions. The volumetric expansion of the hydrogel influences the helical pitch of the CLC, leading to a detectable red shift in the λ_{PBG} . This enables the sensor to exhibit colorimetric changes across the visible spectrum. Initially, the biosensor film displayed a blue color. To optimize lactate sensing, different concentrations of LOx (C_{LOx}) were immobilized on the CLCN-IPN film and tested using a 50 mM lactate (C_{Lactate}) aqueous solution. **Figure 2B** shows that the λ_{PBG} values of the CLCN-IPN_{LOx} film increased linearly with increasing C_{LOx} , reaching equilibrium at 8 μM . The inset photographs demonstrate a visible color shift from blue to yellow as the C_{LOx} concentration increased. **Supplementary Figure 6A** presents the corresponding UV-Vis spectra of CLCN-IPN_{LOx} films with varying C_{LOx} concentrations, displaying a continuous red shift in the λ_{PBG} until C_{LOx} exceeds 8 μM . **Supplementary Figure 6B** illustrates the $\Delta\lambda_{\text{PBG}}$ values, with a maximum shift of 136 nm observed for films immobilized with 8 μM or higher concentrations of C_{LOx} . We selected 8 μM of LOx as the optimal concentration for all experiments unless otherwise specified.

The performance of the CLCN-IPN_{LOx} sensor was evaluated using aqueous solutions of lactate (C_{Lactate}) at varying concentrations. **Figure 2C** shows a redshift in λ_{PBG} values as the concentration of C_{Lactate} increases. Specifically, the λ_{PBG} shifted from 435 to 579 nm, reaching equilibrium at a C_{Lactate} concentration of 50 mM. The inset photographs display a distinct color change of the film, transitioning from blue to brown. The physiological concentration of lactate in human sweat is typically around 25 mM, which corresponds to moderate physical exertion. At this normal physiological level, the sensor exhibits a green color. However, as lactate levels increase, such as during intense exercise or pathological conditions the sensor transitions to yellow and eventually brown, indicating elevated or potentially toxic levels of lactate. This colorimetric shift provides an intuitive, real-time indication of lactate levels in sweat. Lactate is a byproduct of anaerobic

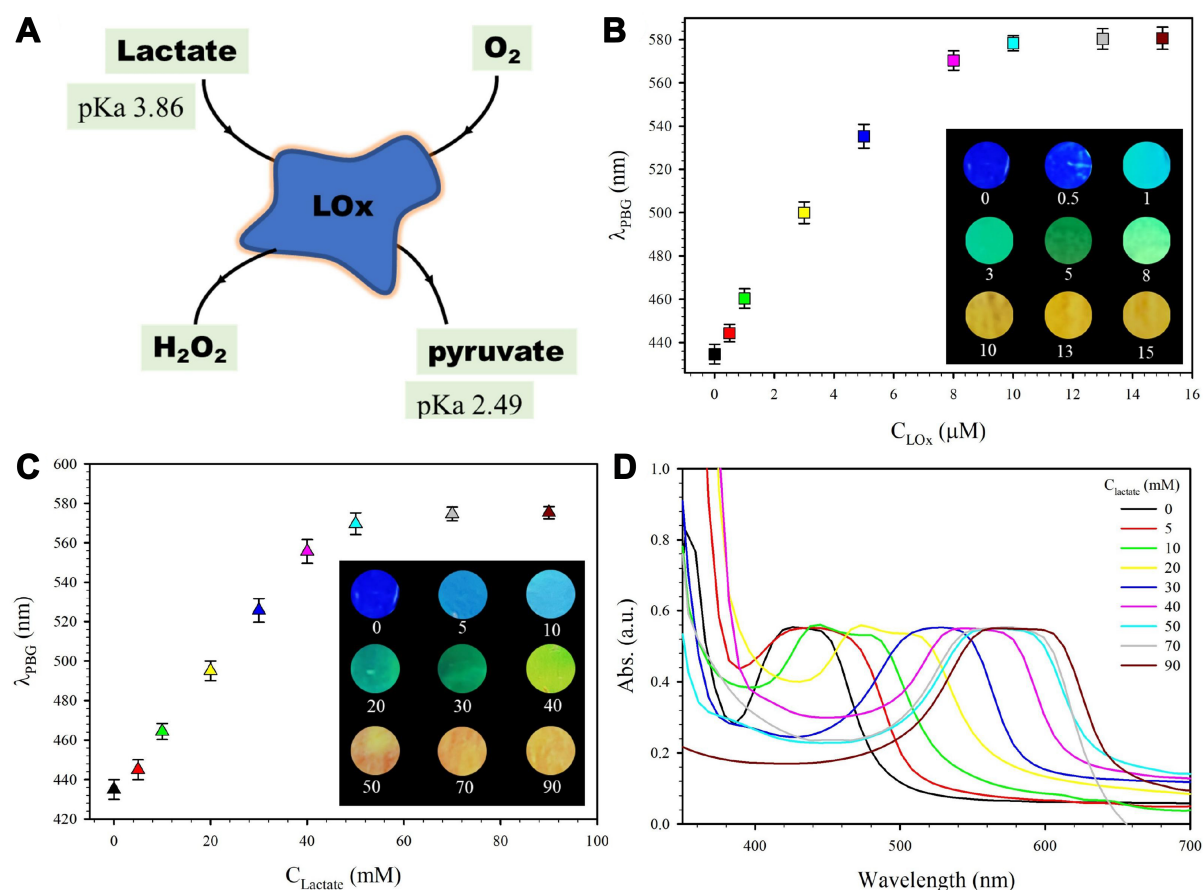


Figure 2. (A) Schematic illustration of the oxidation of lactate by LOx; (B) λ_{PBG} values as a function of LOx concentration; insets show real photographs of CLCN-IPN_{LOx} films immobilized with different concentrations of C_{LOx} ; (C) Redshift in λ_{PBG} values as a function of lactate concentration; insets show photographs of the CLCN-IPN_{LOx} films treated with varying concentrations of $C_{Lactate}$ in aqueous solutions; (D) UV-Vis spectra of the CLCN-IPN_{LOx} films treated with different $C_{Lactate}$ concentrations. Error bars in (B) and (C) represent the standard deviations from triplicate experimental results. CLCN: Cholesteric liquid crystal network; IPN: interpenetrating polymer network; UV-Vis: UV-Visible.

metabolism, and its concentration in sweat can rise significantly during intense exercise or when the body is in a state of oxygen deficit. Elevated lactate levels in sweat are often used as a biomarker for muscle fatigue, hydration status, and metabolic conditions. Monitoring these levels can help assess athletic performance or detect underlying health issues. Figure 2D shows the corresponding UV-Vis spectra of the CLCN-IPN_{LOx} films, where a redshift is observed as lactate concentration increases. Supplementary Figure 6C presents a bar graph of $\Delta\lambda_{PBG}$ values, showing a maximum shift of 144 nm, which is easily distinguishable by the naked eye, making the sensor highly sensitive to lactate concentration changes. The LOD was calculated to be 3.11 mM, with a linear detection range 4–50 mM, as shown in Supplementary Figure 6D. This Figure also serves as a standard calibration curve for determining unknown lactate concentrations. Overall, the sensor's ability to detect lactate levels within the physiological range, as well as its response to elevated concentrations, highlights its potential as a practical tool for real-time monitoring in both sports performance and clinical diagnostics.

Glucose monitoring with the circular photonic CLCN-IPN biosensor film

For glucose monitoring, we utilized a 2.8% reactive CLC mixture combined with an IPN constructed from AA-co-DMAEMA. The choice of the 2.8% reactive CLC mixture was strategic to achieve an initial green

color for the sensor film, as the physiological concentration of glucose in sweat is typically around 1 mM. By tuning the sensor's starting color to green, we ensured that normal glucose levels would not cause a large color shift, while elevated concentrations would result in detectable changes. [Figure 3A](#) presents the UV-Vis spectra of CLCN-IPN films immobilized with varying concentrations of glucose oxidase (C_{Gox}). All the CLCN-IPN_{Gox} films were tested using a 2 mM glucose solution. Glucose oxidase catalyzes the oxidation of glucose to gluconic acid, a process that lowers the local pH. This decrease in pH causes the poly-DMAEMA within the IPN to swell, expanding the helical pitch of the CLC structure, which results in a redshift of the λ_{PBG} . The inset photographs show the CLCN-IPN_{Gox} films treated with $C_{Gox} = 50, 80, \text{ and } 100 \mu\text{M}$, demonstrating a visible color change. [Figure 3B](#) illustrates the linear increase in λ_{PBG} with increasing C_{Gox} , with the optimal concentration determined to be $80 \mu\text{M}$. This concentration was chosen based on the saturation of the redshift beyond $80 \mu\text{M}$. [Supplementary Figure 7A](#) shows a bar graph of $\Delta\lambda_{PBG}$ values vs. C_{Gox} with a maximum $\Delta\lambda_{PBG}$ of 82 nm.

The sensor's response was further tested across a range of glucose concentrations ($C_{Glucose}$). [Figure 3C](#) shows the redshift in λ_{PBG} values as the CLCN-IPN_{Gox} films were exposed to glucose solutions ranging from 0 to 3 mM. The λ_{PBG} shifted from 500 to 582 nm as the $C_{Glucose}$ increased. The inset photographs demonstrate that the color of the film remains green at or below 1 mM glucose, the normal physiological level in sweat, and transitions to yellow at higher concentrations, indicating hyperglycemic conditions. [Figure 3D](#) displays a bar graph of $\Delta\lambda_{PBG}$ values vs. $C_{Glucose}$, while [Supplementary Figure 7B](#) shows the corresponding UV-Vis spectra for the different $C_{Glucose}$. The LOD was calculated to be 0.31 mM, with a linear detection range between 0.9 and 2 mM, as shown in [Supplementary Figure 7C](#), which also serves as the standard calibration curve. Glucose monitoring in sweat is critically important for non-invasive health monitoring, particularly for individuals with diabetes or those at risk of developing metabolic disorders. Sweat glucose levels provide insights into blood glucose trends and can help track glycemic status without the need for invasive blood sampling. The CLCN-IPN_{Gox} sensor, with its ability to detect small changes in $C_{Glucose}$ through visible color shifts, represents a promising tool for real-time glucose monitoring in wearable devices, offering a non-invasive, user-friendly alternative for continuous glucose tracking.

The influence of temperature on the response of the CLCN-IPN_{Gox} film was systematically evaluated. Three CLCN-IPN_{Gox} films were placed in a polystyrene petri dish, which was then filled with DI water, ensuring complete immersion of the films. The initial temperature of the DI water was set to 16°C . As shown in [Supplementary Figure 8A](#), photographs of the films were taken at 16°C , and then the temperature was gradually increased to 30, 40, 50, 55, and finally 60°C . Throughout this temperature range, the color of the films remained unchanged, indicating no visual shift in response to temperature variations. Furthermore, [Supplementary Figure 8B](#) presents the λ_{PBG} values of the corresponding films, which remained constant at 489 nm, identical to the initial measurement at 16°C . These results confirm that temperature variations up to 60°C do not affect the sensor's optical response, ensuring stability under typical environmental conditions.

Fabrication and assembly of a soft wearable biosensor

To fabricate the soft wearable device, a custom-designed resin mold was created. The mold design [[Figure 4A](#)] was generated using AutoCAD software, ensuring precise dimensions and functional components. A SIGA MAX UV 3D printer was used to produce resin mold, which has a diameter of 30 mm and contains a 7 mm diameter sweat collection chamber. Additionally, three reservoirs were incorporated to hold the circular CLCN-IPN biosensor films, each with a diameter of 5 mm. All channels in the design have a thickness of 100 micrometers, allowing for efficient fluid movement. [Figure 4B](#) showcases the soft wearable device filled with dye, demonstrating the functionality of the sweat collection system. The sweat collection chamber gathers sweat and distributes it through inlet channels into the sensor's reservoirs. Once the

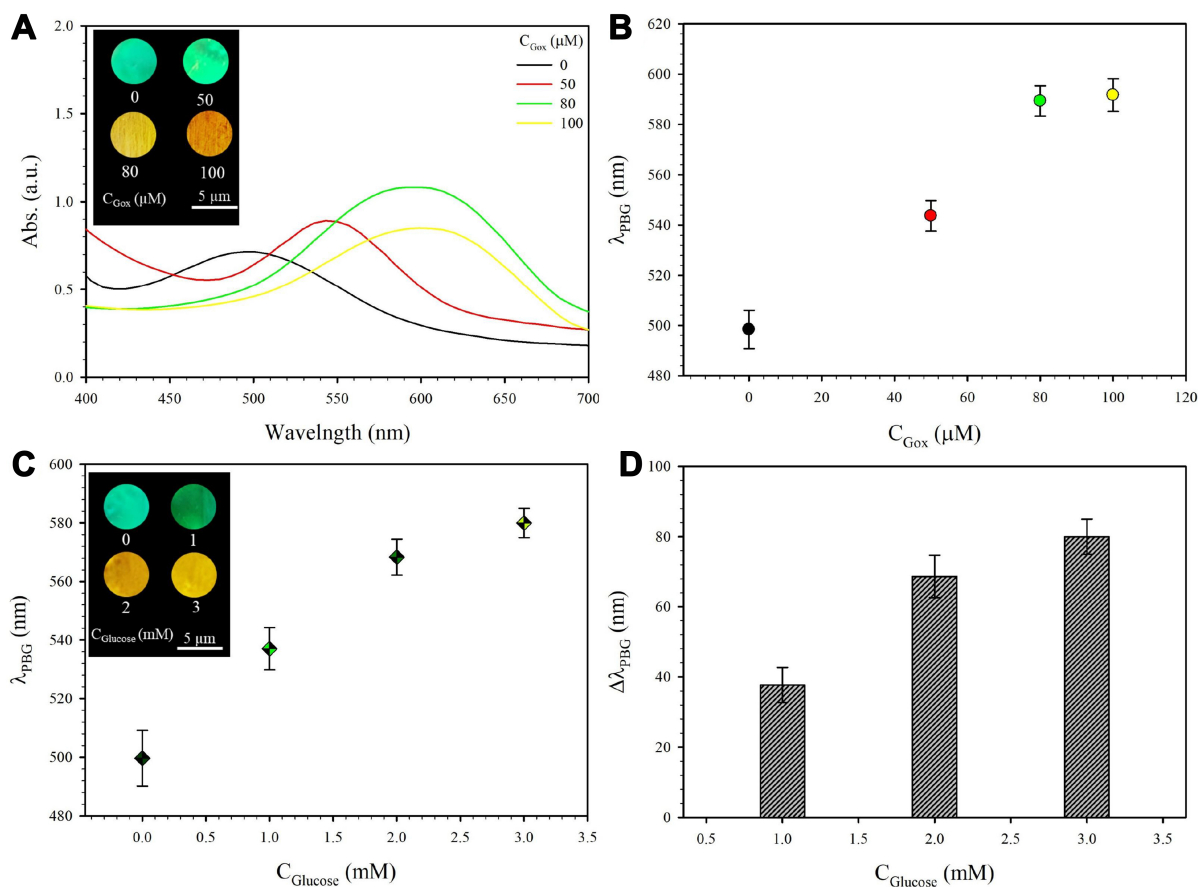


Figure 3. (A) UV-Vis spectra of CLCN-IPN films immobilized with varying concentrations of C_{Gox} , tested using 2 mM glucose aqueous solution for 2 h. The insets show corresponding photographs of the biosensor films; (B) The λ_{PBG} values exhibit an increase with rising C_{Gox} concentration; (C) A linear increase in λ_{PBG} is observed in CLCN-IPN films treated with different concentrations of $C_{Glucose}$. Insets display photographs taken 2 h after the addition of $C_{Glucose}$ aqueous solutions; (D) Bar graph illustrating the $\Delta\lambda_{PBG}$ values as a function of $C_{Glucose}$ concentration in aqueous solutions. Error bars in (B-D) represent the standard deviation from triplicate experimental results. UV-Vis: UV-Visible; CLCN: cholesteric liquid crystal network; IPN: interpenetrating polymer network.

reservoirs are fully filled, excess dye is drained out through the outlet channels, mimicking the sweat flow process. In Figure 4C, a photograph of the patterned resin mold, fabricated using a 3D printer, reveals the clean and precise development of channels and reservoirs. Clear patterning is essential for optimal device performance. Figure 4D highlights the corresponding PDMS patterned layer produced from the mold. The sweat collection chamber is represented as a hole, which will be exposed to human skin to directly collect sweat. The reservoir depth is 200 micrometers, while the total thickness of the PDMS layer is 500 micrometers. This is thin enough to remain flexible, yet robust for wearability. Figure 4E illustrates a high-speed camera image of the PDMS channels, showcasing the pristine formation of the channels. Clean and precise channel development is crucial for ensuring reliable sweat distribution. Figure 4F displays the mold used to produce the top cover layer, which has a thickness of 300 micrometers. This top layer serves to seal the PDMS layer containing the biosensors, preventing sweat evaporation and ensuring stable sensor readings.

Figure 4G illustrates the complete assembly of the soft wearable array biosensors. The assembly includes a top cover layer made of PDMS, along with a patterned layer containing sensor reservoirs. The blue, green, and red colors indicate the positions of the circular CLCN-IPN optical sensor films. These films are

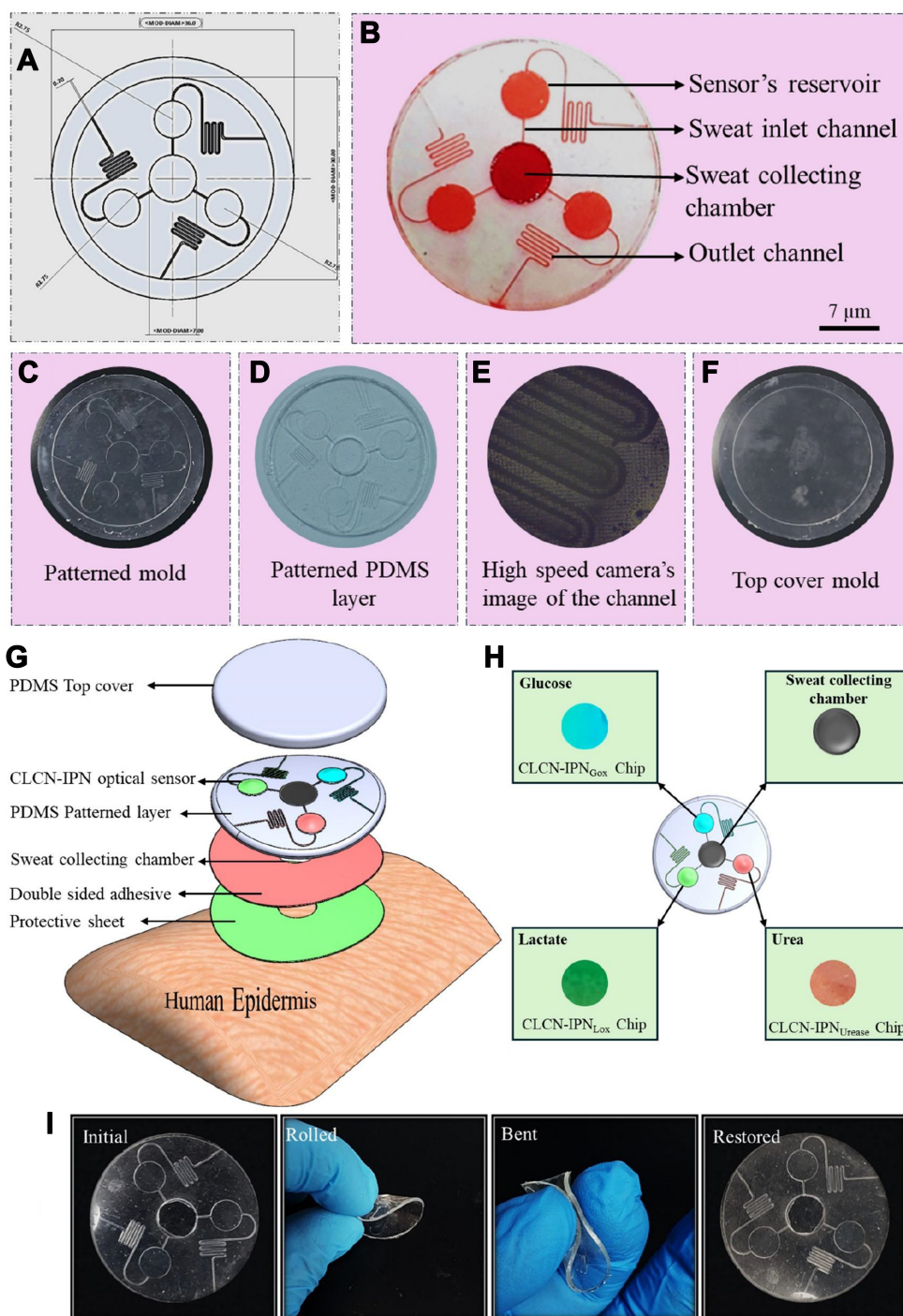


Figure 4. Fabrication and assembly of the soft wearable biosensor device. (A) CAD design of the resin mold for fabricating the soft wearable device, showing the sweat collection chamber and sensor reservoirs; (B) The wearable device filled with dye to demonstrate sweat distribution through inlet channels and drainage through outlet channels; (C) Photograph of the patterned resin mold produced by 3D printing, highlighting the precision of the channels and reservoirs; (D) PDMS patterned layer created by the mold; (E) High-speed camera image showing cleanly developed channels in the PDMS layer; (F) High speed camera's image of the mold which use to produce the top cover layer; (G) Assembly of the wearable biosensor array with blue, green, and red CLCN-IPN optical sensor films for glucose, lactate, and urea detection; (H) Fully assembled device with CLCN-IPN_{Gox}, CLCN-IPN_{Lox}, and CLCN-IPN_{urease} sensors, where the black hole represents the sweat collection chamber; (I) Demonstration of the mechanical stability of the device after deformation, showing its ability to return to its original shape without damage. PDMS: Polydimethylsiloxane; CLCN: cholesteric liquid crystal network; IPN: interpenetrating polymer network.

designed to detect various analytes in sweat. The device is adhered to the human epidermis using medical-grade, double-sided adhesive tape. A hole is precisely cut in the center of the adhesive tape to align with the sweat collection chamber, ensuring direct sweat contact with the sensors. The protective sheet on the tape can be easily removed prior to application on the skin, making it user-friendly and hygienic. **Figure 4H** showcases the fully assembled soft wearable array biosensors, incorporating CLCN-IPN_{GOx}, CLCN-IPN_{Lox}, and CLCN-IPN_{urease} optical sensor films. These films are engineered to selectively detect glucose, lactate, and urea, respectively. The black hole in the center represents the sweat collection chamber, through which sweat flows into the sensor reservoirs. This multi-analyte detection capability allows for comprehensive monitoring of key biomarkers in human sweat, making the device suitable for real-time health monitoring in a non-invasive manner. **Figure 4I** demonstrates the mechanical stability of the wearable device. Even after undergoing significant deformations such as rolling and bending, the device returns to its original shape without any structural damage or compromise in sensor performance. This robustness ensures the device remains functional during daily activities, making it ideal for long-term, real-world applications. This soft, flexible wearable biosensor array not only integrates advanced optical sensor films for real-time monitoring but also offers high mechanical resilience and comfort for continuous wear, showcasing its potential for next-generation health diagnostics.

Off-body artificial sweat analysis

The soft wearable array biosensor was tested using artificial sweat to simulate real-world sweat composition. Two samples were prepared: Sample 1 contained $C_{\text{Glucose}} = 1 \text{ mM}$, $C_{\text{urea}} = 20 \text{ mM}$, and $C_{\text{Lactate}} = 20 \text{ mM}$, reflecting typical physiological concentrations found in human sweat^[53-55]. These concentrations are commonly observed under normal conditions, making Sample 1 an appropriate model for healthy human sweat. The soft wearable array biosensor was mounted on a round PDMS layer, which was connected to a syringe pump for controlled delivery of the artificial sweat. The artificial sweat from Sample 1 was injected at a flow rate of $40 \mu\text{L}/\text{min}$, which corresponds to the typical sweat flow rate from the epidermis during moderate physical activity. This flow rate ensures an accurate simulation of natural sweating, allowing for effective sensor calibration. After 7 min, the biosensor chip was fully saturated. The inset in **Figure 5A** shows the biosensor 2 h after the start of the artificial sweat injection. At normal physiological concentrations, the CLCN-IPN_{GOx}, CLCN-IPN_{Lox}, and CLCN-IPN_{urease} sensors obtained a green color, indicating stable performance. The $\Delta\lambda_{\text{PBG}}$ observed for the CLCN-IPN_{GOx}, CLCN-IPN_{Lox}, and CLCN-IPN_{urease} sensors were 40, 63, and 71 nm, respectively, as shown in the UV-Vis spectra in **Figure 5B**. Sample 2, with elevated concentrations of $C_{\text{urea}} = 50 \text{ mM}$ and $C_{\text{Lactate}} = 50 \text{ mM}$, was designed to mimic conditions commonly associated with metabolic disorders, kidney dysfunction, or dehydration, where abnormal sweat composition serves as a clinical indicator of disease. High lactate levels in sweat may indicate muscle fatigue, hypoxia, or mitochondrial disorders, while elevated urea levels are often linked to renal impairment, including chronic kidney disease, uremia, or imbalances in the body's ability to excrete nitrogenous waste. These abnormal concentrations can reflect disruptions in metabolic or renal function, offering insight into underlying health conditions. The same experimental setup was employed for Sample 2, and the $\Delta\lambda_{\text{PBG}}$ values for the CLCN-IPN_{GOx}, CLCN-IPN_{Lox}, and CLCN-IPN_{urease} sensors were 44, 169, and 140 nm, respectively [**Figure 5C**]. These significant changes were readily observable, with the CLCN-IPN_{Lox} and CLCN-IPN_{urease} sensors turning from blue to orange-red, while the CLCN-IPN_{GOx} sensor remained green, as shown in the inset of **Figure 5C**. The UV-Vis spectra corresponding to Sample 2 are displayed in **Figure 5D**, clearly demonstrating the sensitivity of the biosensor array to elevated metabolite levels. This off-body artificial sweat analysis demonstrates the ability of the soft wearable array biosensor to detect both normal and pathological concentrations of key biomarkers, providing a visually distinguishable response through colorimetric changes and measurable wavelength shifts in real time. This technology has potential applications in non-invasive diagnostics, continuous health monitoring, and personalized medicine.

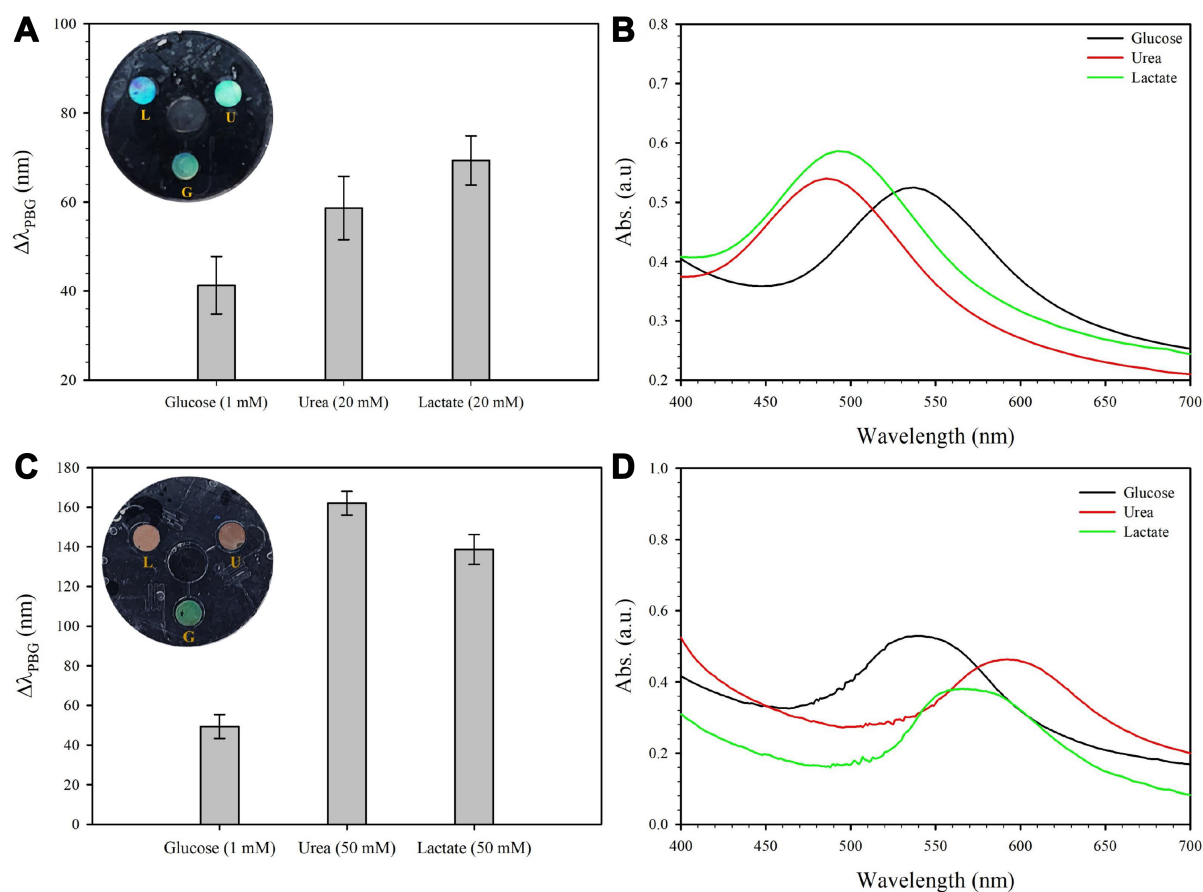


Figure 5. (A) $\Delta\lambda_{PBG}$ values for the CLCN-IPN_{GOx}, CLCN-IPN_{LOx}, and CLCN-IPN_{urease} sensors tested with artificial sweat Sample 1, containing $C_{Glucose} = 1$ mM, $C_{urea} = 20$ mM, and $C_{Lactate} = 20$ mM. The inset shows a real photograph of the soft wearable array biosensor, where L, U, and G correspond to the lactate, urea, and glucose sensors, respectively; (B) UV-Vis spectra corresponding to the CLCN-IPN films tested with Sample 1; (C) $\Delta\lambda_{PBG}$ values for the CLCN-IPN_{GOx}, CLCN-IPN_{LOx}, and CLCN-IPN_{urease} sensors tested with artificial sweat Sample 2, containing $C_{Glucose} = 1$ mM, $C_{urea} = 50$ mM, and $C_{Lactate} = 50$ mM. The inset shows a real photograph of the soft wearable array biosensor after exposure to Sample 2; (D) UV-Vis spectra corresponding to the CLCN-IPN films tested with Sample 2. CLCN: Cholesteric liquid crystal network; IPN: interpenetrating polymer network; UV-Vis: UV-Visible.

To demonstrate the continuous monitoring capability of our sensor, we conducted a 6-hour experiment by continuously passing artificial sweat through the system. The artificial sweat composition included sodium lactate (20 mM), D-glucose (0.5 mM), and urea (21 mM). The first analysis was performed 2 h after initiating artificial sweat injection at a flow rate of 40 μ L/min, followed by measurements at 1-hour intervals. As illustrated in [Supplementary Figure 9](#), the bar graph shows that the measured concentrations of lactate, glucose, and urea remained stable throughout the monitoring period, closely aligning with their actual concentrations. This stability is due to the efficient removal of enzymatic reaction products through the outlet channels of the wearable sensor patch, ensuring a continuous influx of fresh sweat. Consequently, our sensor enables real-time monitoring with sustained performance over an extended period.

Furthermore, we also explored the reusability and long-term stability of the soft wearable array biosensor to assess its potential for extended use. After analyzing Sample 2 of the artificial sweat, the biosensor was carefully recycled. This was done by flushing 5 mL of phosphate-buffered saline (PBS) solution (pH 7) through the system at a flow rate of 40 μ L/min, followed by air drying. After two weeks, we subjected the sensor to the same Sample 2 artificial sweat to test its stability. Impressively, as shown in [Supplementary](#)

Figure 10, the $\Delta\lambda_{\text{PBG}}$ values remained nearly identical to those of a freshly prepared patch. These results highlight the sensor's durability and reliability, indicating that it can maintain its functionality after storage for at least two weeks and be reused multiple times without a loss in performance. This reusability opens exciting possibilities for its application in continuous, long-term sweat monitoring, making it a highly efficient tool for wearable diagnostics.

On-body sweat analysis

To evaluate the real-time performance of the soft, wearable multiplex biosensor for sweat analysis, the device was affixed to the forearm of a healthy volunteer with no prior medical history of glycemia (elevated glucose), uremia (high urea), or hyperlactatemia (high lactate). The volunteer's skin was thoroughly cleansed with water and dried before the biosensor was securely attached using medical-grade adhesive. The patch adhered firmly to the skin throughout the exercise without causing any irritation, ensuring comfort during the testing period. As shown in Figure 6A, both the lactate and urea sensors were blue, while the glucose sensor appeared green prior to exercise. The sensor's sleek design not only enabled seamless adhesion to the skin but also enhanced the aesthetic appeal, offering a stylish integration into wearable technology. Before exercise, the λ_{PBG} for the CLCN-IPN_{urease}, CLCN-IPN_{LOx}, and CLCN-IPN_{Gox} sensors was measured at 430, 432, and 502 nm, respectively, as depicted in Figure 6B. The sweat-collecting chamber, with a diameter of 7 mm, effectively covered an area of 38.4 mm², corresponding to approximately 153 active sweat pores. After 30 min of exercise, the biosensor patch was fully saturated with sweat, as shown in Figure 6C, resulting in a color shift to mint green across all sensors, indicating sweat absorption. Two hours post-exercise, the $\Delta\lambda_{\text{PBG}}$ was analyzed, with shifts of 31, 34, and 16 nm observed for the urea, lactate, and glucose sensors, respectively, as shown in Figure 6D. Using standard curves [Supplementary Figures 5D, 6D, and 7C], the C_{urea}, lactate, and glucose in sweat were quantified at 12.83, 13.1, and 0.39 mM, respectively. These values are within the normal physiological range, confirming the healthy status of the volunteer. This on-body analysis demonstrates the robustness and practicality of the wearable multiplex biosensor for non-invasive monitoring of critical sweat biomarkers such as glucose, urea, and lactate. The real-time colorimetric response, coupled with the biosensor's seamless integration into wearable applications, underscores its potential for continuous health monitoring. The device not only offers a cutting-edge solution for real-time sweat analysis but also integrates user-friendly design, making it an ideal candidate for healthcare, fitness, and personal wellness applications.

CONCLUSION

In this study, we introduced a multiplexed sensing technology integrated into a flexible, wearable microfluidic PDMS device, offering excellent reliability and reproducibility for non-invasive human sweat analysis. The soft wearable patch was engineered to collect sweat from the human epidermis, directing it to each photonic sensor while excess sweat is drained away. The photonic CLCN-IPN flexible film, immobilized with glucose oxidase, LOx, and urease enzymes, enabled selective and enzyme-based detection of glucose, lactate, and urea in sweat. Optical photonic sensing provided a significant advantage by allowing naked-eye visualization of quantitative results through color changes in the film, eliminating the need for complex instrumentation. This technology is not only non-invasive and battery-free but also easy to use in both outdoor and indoor environments, making it highly adaptable for real-world applications. As a proof of concept, the fabricated wearable biosensor array was successfully demonstrated for real-time sweat sensing on a healthy human subject. The combination of optical photonic technology and flexible design marks an important step forward in the development of accessible, user-friendly wearable biosensors. Such an approach has the potential to inspire scalable production of multi-modal sensors for personalized healthcare and pre-diagnosis. Furthermore, this platform can be expanded to incorporate additional biosensors, allowing for the detection of a wider array of analytes.

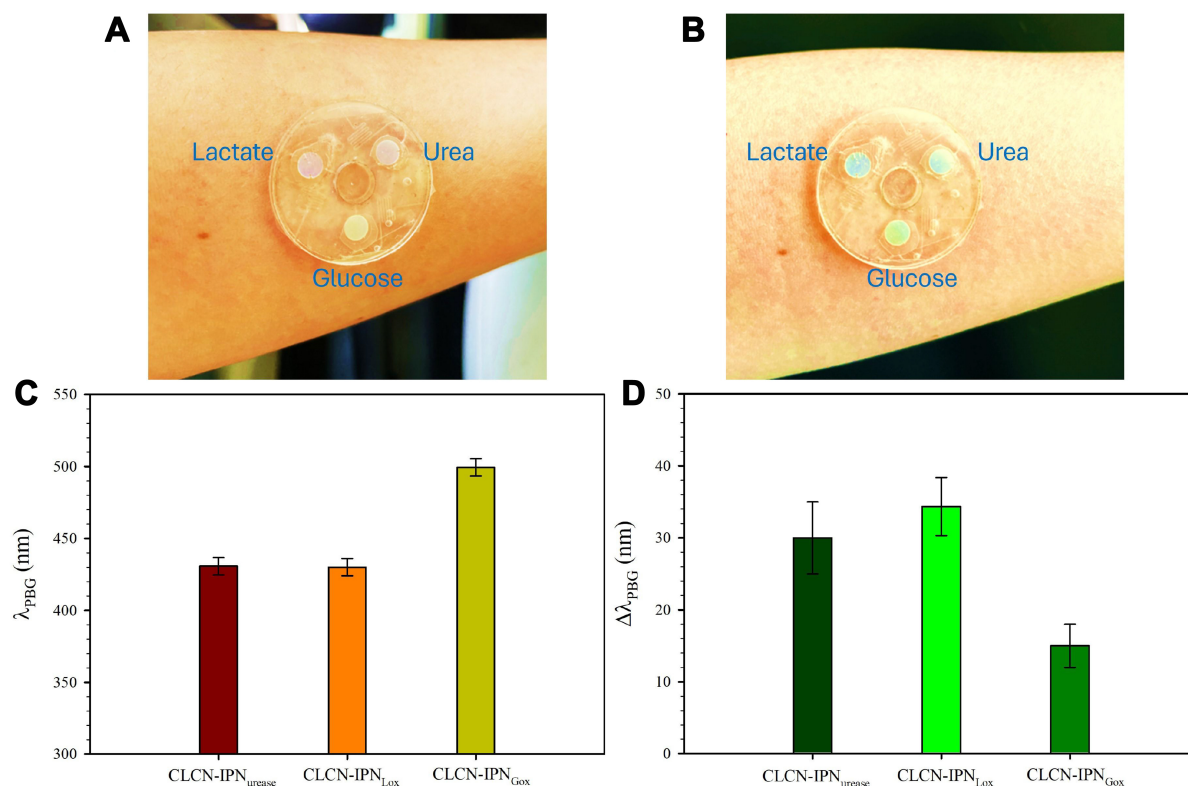


Figure 6. On-body performance of the soft wearable multiplex biosensor for real-time sweat analysis. (A) The wearable biosensor patched onto the volunteer's arm prior to exercise, showing the initial colors: blue for the urea and lactate sensors, and green for the glucose sensor; (B) Initial λ_{PBG} of 430, 432, and 502 nm for the urea, lactate, and glucose sensors, respectively; (C) After 30 min of exercise, the biosensor is fully saturated with sweat, with all sensors shifting to a mint green color; (D) The measured $\Delta\lambda_{PBG}$ of 31, 34, and 16 nm for urea, lactate, and glucose sensors, respectively, corresponding to concentrations of 12.83 mM urea, 13.1 mM lactate, and 0.39 mM glucose, confirming the healthy status of the volunteer.

DECLARATIONS

Authors' contributions

Conceptualization: Hussain, S.; Zourob, M.

Methodology, original draft preparation, and writing: Hussain, S.; Ramadan, Q.; Zourob, M.

Provided administrative, technical, and material support: Zourob, M.

Data analysis: Hussain, S.; Zourob, M.

Conceptualization, funding acquisition, project administration, resources, supervision and writing, review and editing: Hussain, S.; Ramadan, Q.; Zourob, M.

Funding acquisition, Zourob, M.

Availability of data and materials

The data supporting the findings of this study are available within this Article and its [Supplementary Materials](#). Further data are available from the corresponding authors upon request.

Financial support and sponsorship

This work was supported by the Saudi Ministry of Health under project number 1276.

Conflicts of interest

All authors declared that there are no conflicts of interest.

Ethical approval and consent to participate

Ethical approval for this study was granted by the Institutional Review Board (IRB) of Alfaisal University [HA-01-R-058], and written informed consent was obtained from all patients.

Consent for publication

Not applicable.

Copyright

© The Author(s) 2025.

REFERENCES

1. Renbourn, E. T. The history of sweat and the sweat rash from earliest times to the end of the 18th century. *J. Hist. Med. Allied. Sci.* **1959**, *14*, 202-27. [DOI](#) [PubMed](#)
2. Renbourn, E. T. The natural history of insensible perspiration: a forgotten doctrine of health and disease. *Med. Hist.* **1960**, *4*, 135-52. [DOI](#) [PubMed](#) [PMC](#)
3. El-Radhi AS. History of fever. In *Clinical Manual of Fever in Children*, Springer, Cham, 2018; pp. 287-97. [DOI](#)
4. Baker, L. B.; Wolfe, A. S. Physiological mechanisms determining eccrine sweat composition. *Eur. J. Appl. Physiol.* **2020**, *120*, 719-52. [DOI](#) [PubMed](#) [PMC](#)
5. Polychronopoulou, E.; Braconnier, P.; Burnier, M. New insights on the role of sodium in the physiological regulation of blood pressure and development of hypertension. *Front. Cardiovasc. Med.* **2019**, *6*, 136. [DOI](#) [PubMed](#) [PMC](#)
6. Yuan, X.; Li, C.; Yin, X.; et al. Epidermal wearable biosensors for monitoring biomarkers of chronic disease in sweat. *Biosensors* **2023**, *13*, 313. [DOI](#) [PubMed](#) [PMC](#)
7. Davis, P. B. Cystic fibrosis since 1938. *Am. J. Respir. Crit. Care. Med.* **2006**, *173*, 475-82. [DOI](#) [PubMed](#)
8. Mattar, A. C.; Leone, C.; Rodrigues, J. C.; Adde, F. V. Sweat conductivity: an accurate diagnostic test for cystic fibrosis? *J. Cyst. Fibros.* **2014**, *13*, 528-33. [DOI](#)
9. Collie, J. T.; Massie, R. J.; Jones, O. A.; LeGrys, V. A.; Greaves, R. F. Sixty-five years since the New York heat wave: advances in sweat testing for cystic fibrosis. *Pediatr. Pulmonol.* **2014**, *49*, 106-17. [DOI](#) [PubMed](#)
10. Farrell, P. M.; White, T. B.; Derichs, N.; Castellani, C.; Rosenstein, B. J. Cystic fibrosis diagnostic challenges over 4 decades: historical perspectives and lessons learned. *J. Pediatr.* **2017**, *181S*, S16-26. [DOI](#)
11. Hussain, J. N.; Mantri, N.; Cohen, M. M. Working up a good sweat - the challenges of standardising sweat collection for metabolomics analysis. *Clin. Biochem. Rev.* **2017**, *38*, 13-34. [PubMed](#) [PMC](#)
12. Yeung, K. K.; Huang, T.; Hua, Y.; Zhang, K.; Yuen, M. M. F.; Gao, Z. Recent advances in electrochemical sensors for wearable sweat monitoring: a review. *IEEE. Sensors. J.* **2021**, *21*, 14522-39. [DOI](#)
13. Chung, M.; Fortunato, G.; Radacsi, N. Wearable flexible sweat sensors for healthcare monitoring: a review. *J. R. Soc. Interface.* **2019**, *16*, 20190217. [DOI](#) [PubMed](#) [PMC](#)
14. Huestis, M. A.; Oyler, J. M.; Cone, E. J.; Wstadik, A. T.; Schoendorfer, D.; Joseph, R. E. J. Sweat testing for cocaine, codeine and metabolites by gas chromatography-mass spectrometry. *J. Chromatogr. B. Biomed. Sci. Appl.* **1999**, *733*, 247-64. [DOI](#) [PubMed](#)
15. Gao, W.; Brooks, G. A.; Klonoff, D. C. Wearable physiological systems and technologies for metabolic monitoring. *J. Appl. Physiol.* **2018**, *124*, 548-56. [DOI](#) [PubMed](#)
16. Xu, J.; Fang, Y.; Chen, J. Wearable biosensors for non-invasive sweat diagnostics. *Biosensors* **2021**, *11*, 245. [DOI](#) [PubMed](#) [PMC](#)
17. Taylor, J. R.; Watson, I. D.; Tames, F. J.; Lowe, D. Detection of drug use in a methadone maintenance clinic: sweat patches versus urine testing. *Addiction* **1998**, *93*, 847-53. [DOI](#)
18. Kintz, P.; Tracqui, A.; Mangin, P.; Edel, Y. Sweat testing in opioid users with a sweat patch. *J. Anal. Toxicol.* **1996**, *20*, 393-7. [DOI](#)
19. De Giovanni N, Fucci N. The current status of sweat testing for drugs of abuse: a review. *Curr. Med. Chem.* **2013**, *20*, 545-61. [DOI](#) [PubMed](#)
20. Bariya, M.; Nyein, H. Y. Y.; Javey, A. Wearable sweat sensors. *Nat. Electron.* **2018**, *1*, 160-71. [DOI](#)
21. Currano, L. J.; Sage, F. C.; Hagedon, M.; Hamilton, L.; Patrone, J.; Gerasopoulos, K. Wearable sensor system for detection of lactate in sweat. *Sci. Rep.* **2018**, *8*, 15890. [DOI](#) [PubMed](#) [PMC](#)
22. Brothers, M. C.; DeBrosse, M.; Grigsby, C. C.; et al. Achievements and challenges for real-time sensing of analytes in sweat within wearable platforms. *Acc. Chem. Res.* **2019**, *52*, 297-306. [DOI](#)
23. Childs, A.; Mayol, B.; Lasalde-Ramírez, J. A.; Song, Y.; Sempionatto, J. R.; Gao, W. Diving into sweat: advances, challenges, and future directions in wearable sweat sensing. *ACS. Nano.* **2024**, *18*, 24605-16. [DOI](#) [PubMed](#)
24. Ma, S.; Wan, Z.; Wang, C.; et al. Ultra-sensitive and stable multiplexed biosensors array in fully printed and integrated platforms for

- reliable perspiration analysis. *Adv. Mater.* **2024**, *36*, e2311106. DOI PubMed
25. Alsunaidi, B.; Althobaiti, M.; Tamal, M.; Albaker, W.; Al-Naib, I. A review of non-invasive optical systems for continuous blood glucose monitoring. *Sensors* **2021**, *21*, 6820. DOI PubMed PMC
 26. Manjakkal, L.; Yin, L.; Nathan, A.; Wang, J.; Dahiya, R. Energy autonomous sweat-based wearable systems. *Adv. Mater.* **2021**, *33*, e2100899. DOI PubMed PMC
 27. Xiao, G.; He, J.; Qiao, Y.; et al. Facile and low-cost fabrication of a thread/paper-based wearable system for simultaneous detection of lactate and pH in human sweat. *Adv. Fiber. Mater.* **2020**, *2*, 265-78. DOI
 28. Bandodkar, A. J.; Gutruf, P.; Choi, J.; et al. Battery-free, skin-interfaced microfluidic/electronic systems for simultaneous electrochemical, colorimetric, and volumetric analysis of sweat. *Sci. Adv.* **2019**, *5*, eaav3294. DOI PubMed PMC
 29. Promphet, N.; Rattanawaleedirojn, P.; Siralertmukul, K.; et al. Non-invasive textile based colorimetric sensor for the simultaneous detection of sweat pH and lactate. *Talanta* **2019**, *192*, 424-30. DOI
 30. Wang, J.; Luo, Y.; Zhou, Z.; Xiao, J.; Xu, T.; Zhang, X. Epidermal wearable optical sensors for sweat monitoring. *Commun. Mater.* **2024**, *5*, 518. DOI
 31. Nie, N.; Gong, X.; Gong, C.; et al. A wearable thin-film hydrogel laser for functional sensing on skin. *Anal. Chem.* **2024**, *96*, 9159-66. DOI
 32. Chen, S.; Qiao, Z.; Niu, Y.; et al. Wearable flexible microfluidic sensing technologies. *Nat. Rev. Bioeng.* **2023**, *1*, 950-71. DOI
 33. Mohan, A.; Rajendran, V.; Mishra, R. K.; Jayaraman, M. Recent advances and perspectives in sweat based wearable electrochemical sensors. *TrAc. Trends. Anal. Chem.* **2020**, *131*, 116024. DOI
 34. Ghaffari, R.; Yang, D. S.; Kim, J.; et al. State of sweat: emerging wearable systems for real-time, noninvasive sweat sensing and analytics. *ACS. Sens.* **2021**, *6*, 2787-801. DOI PubMed PMC
 35. Bandodkar, A. J.; Jeang, W. J.; Ghaffari, R.; Rogers, J. A. Wearable sensors for biochemical sweat analysis. *Annu. Rev. Anal. Chem.* **2019**, *12*, 1-22. DOI PubMed
 36. Choi, J.; Ghaffari, R.; Baker, L. B.; Rogers, J. A. Skin-interfaced systems for sweat collection and analytics. *Sci. Adv.* **2018**, *4*, eaar3921. DOI PubMed PMC
 37. Zhang, S.; Tan, R.; Xu, X.; Iqbal, S.; Hu, J. Fibers/textiles-based flexible sweat sensors: a review. *ACS. Mater. Lett.* **2023**, *5*, 1420-40. DOI
 38. Parrilla, M.; Guinovart, T.; Ferré, J.; Blondeau, P.; Andrade, F. J. A wearable paper-based sweat sensor for human perspiration monitoring. *Adv. Healthc. Mater.* **2019**, *8*, e1900342. DOI PubMed
 39. Song, J.; Shi, R.; Bai, X.; Algadi, H.; Sridhar, D. An overview of surface with controllable wettability for microfluidic system, intelligent cleaning, water harvesting, and surface protection. *Adv. Compos. Hybrid. Mater.* **2023**, *6*, 603. DOI
 40. Hussain, S.; Zourob, M. Solid-state cholesteric liquid crystals as an emerging platform for the development of optical photonic sensors. *Small* **2024**, *20*, e2304590. DOI PubMed
 41. Myung, D.; Hussain, S.; Park, S. Photonic calcium and humidity array sensor prepared with reactive cholesteric liquid crystal mesogens. *Sens. Actuators. B. Chem.* **2019**, *298*, 126894. DOI
 42. Stumpel, J. E.; Gil, E. R.; Spoelstra, A. B.; Bastiaansen, C. W. M.; Broer, D. J.; Schenning, A. P. H. J. Stimuli-responsive materials based on interpenetrating polymer liquid crystal hydrogels. *Adv. Funct. Mater.* **2015**, *25*, 3314-20. DOI
 43. Wang, T.; Zhao, J.; Wu, L.; Liu, W.; Li, Y.; Yang, Y. Polymer network film with double reflection bands prepared using a thermochromic cholesteric liquid crystal mixture. *ACS. Appl. Mater. Interfaces.* **2024**, *16*, 18001-7. DOI
 44. Hussain, S.; Park, S. Y. Photonic cholesteric liquid-crystal elastomers with reprogrammable helical pitch and handedness. *ACS. Appl. Mater. Interfaces.* **2021**, *13*, 59275-87. DOI PubMed
 45. Yeh, T. Y.; Liu, M. F.; Lin, R. D.; Hwang, S. J. Alcohol selective optical sensor based on porous cholesteric liquid crystal polymer networks. *Molecules* **2022**, *27*, 773. DOI PubMed PMC
 46. Hussain, S.; Park, S. Y. Sweat-based noninvasive skin-patchable urea biosensors with photonic interpenetrating polymer network films integrated into PDMS chips. *ACS. Sens.* **2020**, *5*, 3988-98. DOI PubMed
 47. Hussain, S.; Al-Tabban, A.; Zourob, M. Aptameric photonic structure-based optical biosensor for the detection of microcystin. *Biosens. Bioelectron.* **2024**, *260*, 116413. DOI PubMed
 48. Hussain, S.; Park, S. Optical glucose biosensor based on photonic interpenetrating polymer network with solid-state cholesteric liquid crystal and cationic polyelectrolyte. *Sens. Actuators. B. Chem.* **2020**, *316*, 128099. DOI
 49. Noh, K.; Park, S. Biosensor array of interpenetrating polymer network with photonic film templated from reactive cholesteric liquid crystal and enzyme-immobilized hydrogel polymer. *Adv. Funct. Mater.* **2018**, *28*, 1707562. DOI
 50. Munir, S.; Hussain, S.; Park, S. Y. Patterned photonic array based on an intertwined polymer network functionalized with a nonenzymatic moiety for the visual detection of glucose. *ACS. Appl. Mater. Interfaces.* **2019**, *11*, 37434-41. DOI
 51. Zhang, P.; de, H. L. T.; Debije, M. G.; Schenning, A. P. H. J. Liquid crystal-based structural color actuators. *Light. Sci. Appl.* **2022**, *11*, 248. DOI PubMed PMC
 52. Laochai, T.; Moonla, C.; Moon, J.; et al. Touch-based potentiometric sensors for simultaneous detection of urea and ammonium from fingertip sweat. *Sens. Actuators. B. Chem.* **2024**, *413*, 135898. DOI
 53. Lee, H.; Song, C.; Hong, Y. S.; et al. Wearable/disposable sweat-based glucose monitoring device with multistage transdermal drug delivery module. *Sci. Adv.* **2017**, *3*, e1601314. DOI PubMed PMC
 54. Salatiello, S.; Spinelli, M.; Cassiano, C.; Amoresano, A.; Marini, F.; Cinti, S. Sweat urea bioassay based on degradation of Prussian

- Blue as the sensing architecture. *Anal. Chim. Acta.* **2022**, *1210*, 339882. DOI
55. Xuan, X.; Pérez-Ràfols, C.; Chen, C.; Cuartero, M.; Crespo, G. A. Lactate biosensing for reliable on-body sweat analysis. *ACS. Sens.* **2021**, *6*, 2763-71. DOI PubMed PMC